Published in
Review of Scientific Instruments 78, issue 103109, 1-9, 2007
which should be used for any reference to this work

An electrostatic glass actuator for ultrahigh vacuum: A rotating light trap for continuous beams of laser-cooled atoms

F. Füzesi,[a] A. Jornod,[b] and P. Thomann[c]
Observatoire cantonal de Neuchâtel (ON), rue de l'Observatoire 58, CH-2000 Neuchâtel, Switzerland

M. D. Plimmer[d] and G. Dudle[e]
Federal Office of Metrology (METAS), Lindenweg 50, CH-3003 Bern-Wabern, Switzerland

R. Moser,[f] L. Sache,[g] and H. Bleuler[h]
Laboratory of Robotic Systems (LSRO), EPFL Lausanne, CH-1015 Lausanne, Switzerland

This article describes the design, characterization, and performance of an electrostatic glass actuator adapted to an ultrahigh vacuum environment (10^{-8} mbar). The three-phase rotary motor is used to drive a turbine that acts as a velocity-selective light trap for a slow continuous beam of laser-cooled atoms. This simple, compact, and nonmagnetic device should find applications in the realm of time and frequency metrology, as well as in other areas of atomic, molecular physics and elsewhere.

I. INTRODUCTION

Electrostatic glass actuators are novel, entirely nonmagnetic devices allowing the translation and positioning of loads. Their principle, based on the existence of a static induced charge, was demonstrated several years ago[1] and a detailed description of the prototype can be found in Ref. 2. The application of such a device to precise positioning with three degrees of freedom was proposed and tested shortly thereafter.[3] An analytical and experimental description of the forces and torques present in this type of actuator was also carried out.[4] Advances in precise positioning using the motor were subsequently obtained.[5] All of that work, however, dealt with performance in air or under moderate vacuum ($>10^{-3}$ mbar). Now, in a collaboration between our groups at EPFL, ON, and METAS, such an actuator specifically designed for a UHV environment (Fig. 1) has been developed and characterized.

Under these conditions, the friction due to the surrounding gas is negligible. Thus, measurements of the decay constant once the driving torque is removed provide direct information on the frictional forces present in the motor itself. Furthermore, under UHV conditions, one can apply higher electric fields than in air, which allows greater torques. On the other hand, the viscous drag of the surrounding gas at $>10^{-4}$ mbar that can help stabilize rotation is absent at higher vacuum, making mechanical design more critical if vibrations are to be avoided.

While there are many possible uses for UHV-compatible nonmagnetic actuators, the present case relates to atomic physics. Here, the implementation of the electrostatic motor in a future primary frequency standard, a cold-atom continuous fountain clock, represents a major step forward in this area of metrology and opens the way to other applications such as atom interferometry.[6]

The remainder of this article is subdivided as follows. In Sec. II we recall the theory of operation of the electrostatic glass actuator. The following section (Sec. III) describes the need for this type of motor in the development of a state-of-the-art atomic clock. The characterization and performance of a UHV-compatible prototype are described in Sec. IV. The fifth section contains the conclusions.

II. THEORY OF THE ELECTROSTATIC MOTOR

When a sample of glass is placed in an electric field, an imminent polarization is observed, as with any dielectric. In addition, however, if the field is applied for a period of the order of seconds, a further polarization takes place. This secondary polarization has a rise and decay constant of several seconds and its induced charge distributions linger long after the applied electric field has been switched off. Crucially, these charges are almost immobile and thus allow the glass to be propelled via a moving electric field.

The electrostatic glass motor (EGM) is a device based on this principle. From a classification point of view, the EGM lies between asynchronous induction and synchronous machines: induced charges on the rotor have such a small mobility that, once induced by noncontact induction, they behave like permanent charges, allowing for a synchronous motor regime. The rotor, consisting of a specific silica-based glass blend, is initially electrically neutral. In a first phase,

[a]Present address: SGFC S.A., Domaine de Boislande, Route de St-Cergue 16, CH-1276 Gingins, Switzerland.
[b]Present address: ASULAB, a Division of Swatch Group Research and Development Ltd., rue des Sors 3, CH-2074 Marin, Switzerland.
[c]Present address: LTF-IMT, Université de Neuchâtel, rue A.-L. Breguet 1, CH-2000 Neuchâtel, Switzerland.
[d]Present address: LNE-INM-CNAM, 61 rue du Landy, F-93210 La Plaine-Saint Denis, France.
[e]Electronic mail: gregor.dudle@metas.ch
[f]Also at ALSTOM (Switzerland) Ltd. CH-5400 Baden, Switzerland.
[g]Also at RUAG Aerospace (Switzerland) Ltd. CH-1260, Nyon, Switzerland.
[h]URL: http://www.epfl.ch/

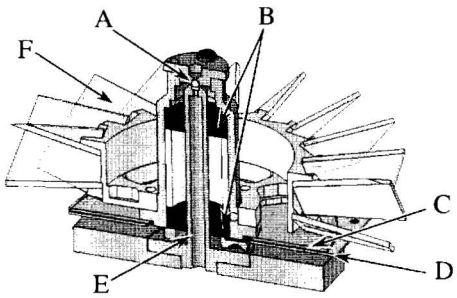

FIG. 1. (Color online) Section through electrostatically driven light trap turbine for the configuration installed in the atomic fountain clock FOCS-1. Key: (A) thrust bearing, (B) ball races, (C) glass rotor, (D) stator, (E) spindle, and (F) glass blades.

the glass rotor is subjected to a static electrostatic field produced by the stator for a several seconds to a few minutes depending on the particular design parameters. During this period, a charge pattern is induced on the glass surface, basically mirroring that of the static stator field. These charges, whose induction has a rise and decay constant of the order of *tens* of seconds, are temporarily bound to their respective positions on the glass rotor and can therefore be used to propel the rotor using a moving electrostatic field. Figure 2 explains the typical charge dynamics.

It is the charge difference in Fig. 2 that is used for attraction or repulsion between rotor and stator. Based on this principle, a rotary motor was developed and its structure is presented in Fig. 3. A stator substrate (3) with imprinted stator electrodes and connection pads is used to apply three different electrode phases, allowing for a rotary electric field. The glass rotor (1) is held at a constant gap g above the stator electrode by means of a bearing (2). The three connection leads (4) are soldered onto the stator.

To set the machine in motion, the voltages on all electrodes—mutually phase shifted by 120°—are first kept at a constant dc level, in order to allow the rotor to charge up. The necessary charging time depends on the applied voltage, the gap g, the glass blend, and the design of the stator electrode. In atmospheric conditions, the applied voltages are about 1 kV and the necessary charging time around 10 s. After this charging period, the rotor bears an "imprinted" mirror image of the stator charge distribution. If now a rotary electric field is applied to the stator, the relatively stable

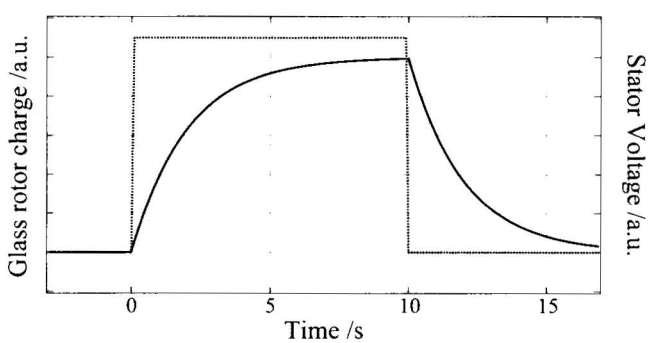

FIG. 2. Charge dynamics during the polarisation phase of a typical electrostatic glass motor.

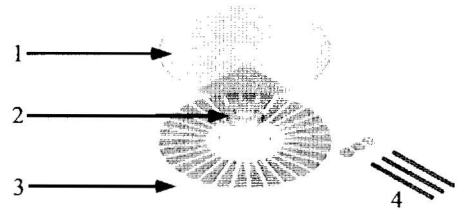

FIG. 3. (Color online) Exploded view of the structure of the rotary electrostatic glass motor in its simplest form. Key: (1) glass rotor, (2) bearing, (3) substrate, and (4) connection leads for three phases.

charges corresponding to the plateau of Fig. 2 cannot follow the moving field yet are attracted by it and therefore start to drag the rotor along: the rotor starts to turn.

Figure 4 shows the timing of the voltages applied to the stator. The voltages of the three electrode phases A, B, and C are kept at a constant level for between 10 s and 2 min. At the end of this charging period, the voltages are applied in a sinusoidal manner, mutually shifted by 120°. Since strongly polarized regions in the glass are attracted by high electric field regions as determined by the voltages applied to the stator, no depolarization of the rotor will take place and it will continue to turn. Note that only the relatively immobile slow induced polarization contributes to the rotation.

An interesting feature of the EGM is its ripple-free rotation, an attractive characteristic that distinguishes it from stepper motors where cogging is an intrinsic property. This phenomenon has been observed in earlier studies showing that the ripple decreases with the same time constant as that associated with charging.

In the simplest method of operation, after the charging period, a fixed rotation speed ω_0 is imposed. To begin with, a significant speed ripple is observed, resulting in a variation $\Delta\omega$ of the rotation speed around its imposed mean value of ω_0. This speed ripple is physically explained with the fact that, at rest, neither rotor nor stator has a sinusoidal charge distribution. After typically 30 s, this speed ripple disappears with a time constant identical to that observed during charging. This phenomenon is due to the now sinusoidal charge distributions on both rotor and stator. (Note that the operation of the device described in Sec. IV is actually more com-

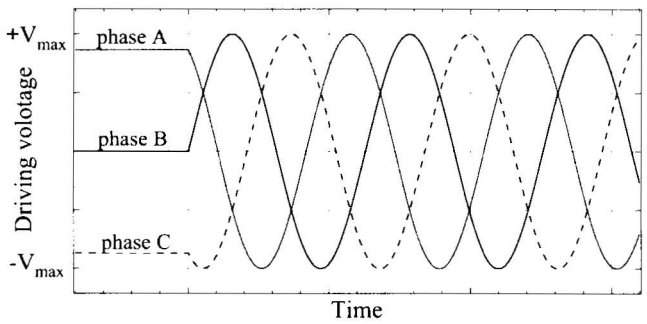

FIG. 4. The simplest scheme for charging and operation of the electrostatic glass motor. After a static polarisation phase, three fixed-frequency sinusoidal voltages, dephased by 120°, are applied to neighboring electrodes of the stator. In the prototype described in Sec. IV, the driving frequency is actually ramped up from zero.

plex since first the driving frequency is slowly increased from zero and second the motor rotates under UHV).

This entirely new type of actuator is quite different from all other known types of electric motors. While certainly not as powerful as electromagnetic motors, the EGM has enough torque to overcome the friction of conventional rotor bearings. There is neither torque ripple nor parasitic radial forces. The axial (thrust) forces are of the order of magnitude of the torque generating forces, i.e., they are measurable but relatively weak. No sensors or other complex components are necessary, smooth constant velocity rotation can be achieved in open loop. The only drawback is the relatively weak torque which means that speed changes (both acceleration or deceleration) typically take between a few tens of seconds and several minutes. Already in air or under moderate vacuum, rotational speeds up to several 1000 rpm have been obtained.[1–5] The basic EGM has an extremely simple structure and, since a wide choice of temperature resistant materials is available, it is possible to obtain fully UHV-compatible designs, e.g., for the present application to drive a light trap. An additional advantage of this new type of motor is the absence of magnetic fields essential to applications in atomic and molecular physics discussed in the next section.

III. APPLICATION TO ATOMIC AND MOLECULAR PHYSICS

The current Système International (S.I.) definition of the second stipulates that the microwave absorption frequency of an unperturbed ^{133}Cs atom at rest be equal to exactly 9 192 631 770 Hz. Since a detailed description of the principle of state-of-the-art atomic clocks is beyond the scope of this article, the interested reader is referred to the review by Wynands and Weyers (2005).[7] Suffice to say that, currently, the best primary time standards are laser-cooled atomic fountain clocks in which the atoms undergo two successive microwave interrogations separated by about 0.5 s. This yields resonance linewidths close to 1 Hz. The fractional accuracy of such devices is reported to be 10^{-15} or better, e.g., Refs. 8 and 9. All but two existing fountain clocks use pulsed capture, vertical launch, interrogation, and detection of dense bunches of cold atoms. In such devices, the existence of a density-related collisional frequency shift[10–12] leads to an inevitable trade-off between stability and accuracy. In addition, the sequential operation of the device implies a reduction in stability via intermodulation noise due to the folding in of the power spectrum of the local oscillator phase fluctuations.[13] A few fountain clocks currently operating use real-time measurement of atomic density and ultrahigh stability local oscillators[14] to circumvent these problems. Another strategy relies upon careful control of hyperfine level populations to cancel the collisional shift.[15]

An alternative approach is to use a *continuous* fountain (Fig. 5) where the microwave cavity consists of two spatially separated regions traversed by the atoms in a parabolic flight. Because for an identical signal-to-noise ratio compared with a pulsed fountain, the required atomic density is about $\simeq 100$ times lower and the longitudinal temperature much higher (70 μK versus 2 μK), collisional shifts are greatly reduced.

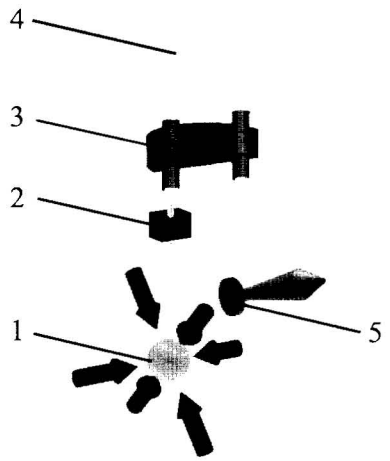

FIG. 5. (Color online) Sketch of the continuous fountain. (1) Source of continuous beam of laser-cooled atoms; (2) light trap; (3) microwave cavity; (4) parabola formed by the continuous flux of atoms; (5) optical detection.

Furthermore, by the use of an appropriate microwave interrogation scheme, intermodulation noise can be made negligible.[13,16] Finally, the composition of the uncertainty budget is somewhat different for continuous and pulsed fountain standards, which makes the former a useful metrological asset. To provide a continuous flux, however, the laser beams used for cooling, state preparation, and detection must remain switched on permanently. Laser-induced atomic fluorescence from the source region, if not attenuated, would lead to a shift of the microwave transition frequency at the 10^{-12} level, i.e., 1000 times the target accuracy. It is thus indispensable to shield the atoms in the microwave interaction region from this light. Two such continuous fountain clocks (FOCS-1 and FOCS-2), built at ON, have now been installed at METAS.[6] They incorporate a rotating light trap based on a turbine whose filter glass blades (Schott-type BG42, thickness of 1 mm), inclined at 45° to the atomic trajectory. The rotation speed of the blades is 17 Hz such that, at the point of impact of the atomic beam, the tangential velocity matches the mean atomic speed of 3.6 ms^{-1}. The glass absorbs most of the light at 852 nm and specularly reflects the remainder into a graphite trap. Although the effectiveness of such a light attenuator has already been demonstrated,[17] its reliable implementation in an atomic clock had been hampered by numerous, different failures of electromagnetic stepper motors used to drive the turbine. The absence of suitable nonmagnetic vacuum feedthroughs makes it necessary to operate the motor under UHV. In addition, even when they do manage to run for long periods under high vacuum without stopping, electromagnetic motors produce magnetic fields that have to be shielded if the accuracy of the atomic clock is not to be compromised. The development of the electrostatic actuator described in this article essentially solves these problems. It opens the way to the use of continuous beams of cold atoms in time and frequency metrology and possibly atom interferometry. In the next section, we present the design criteria, the diagnostic

techniques, and the results obtained therewith.

IV. DESIGN, CHARACTERIZATION, AND PERFORMANCE

The need for a primary atomic clock to run continuously for months on end makes the design requirements of any motor rather severe. The device must be nonmagnetic, UHV compatible, resist baking to 100 °C, and be inert to Cs vapor at 10^{-8} mbar. The turbine should rotate uninterrupted at 17 Hz for several months, ideally for up to two years. In the event of the motor's stopping for any reason, one must be able to restart it remotely. In addition, the present light trap had to be small enough to fit into the space available in an existing fountain clock (a cylindrical volume of height and diameter of 90 mm).

A. Design

The initial design was based on earlier prototypes[1,4] but with elements replaced to make the device nonmagnetic and UHV compatible. The essential goal was to provide a high enough torque (about 10^{-4} N m) to achieve and maintain the desired rotation speed. This depends on the friction present in the system. In addition, vibrations had to be minimized via the use of appropriate bearings though, as shown below, this increased friction albeit acceptably. Electrical and mechanical modifications were made in response to performance under vacuum until the rotation frequency of 17 Hz could be obtained routinely and random stoppages or short circuits avoided.

1. Mechanical design

The basic actuator consists of a base plate supporting an alumina stator of 60×60 mm^2, on which a series of 180 silver-palladium radial electrodes (internal diameter of 24 mm, external 58 mm) was deposited using screen printing with electrical connections on the underside. This constitutes 60 poles for three-phase operation. The interelectrode spacing at the circumference is 300 μm. The rotor consists of a 58 mm diameter glass plate (Ohara TS-10SX) to which the turbine is attached. The ensemble is suspended above the stator and pivots around a central titanium spindle. The mass of the load was $\leq$70 g, depending on the configuration employed (see below), and its moment of inertia is $I=3.4\times10^{-5}$ kg m^2. Four different configurations were tested: (i) with a single thrust bearing, (ii) with a thrust bearing and a single ball race, (iii) with a thrust bearing and two ball races (Fig. 1), and (iv) with two ball races but no thrust bearing. In configurations (i)—(iii), the weight of the turbine was supported by a Comadur 1/16 in. (1.59 mm) diameter, class 5 silicon nitride (Si_3N_4) bearing. For configuration (i), this bearing rested on a sapphire cuvette (Comadur U-11953.061) attached to the top of the spindle. In versions (ii) and (iii) with both thrust bearing and ball race(s) (NSK Spacea 605LZZC3-HMST4 with molybdenum disulphide lubricant), a sapphire flat (Comadur 11950.179) was used instead as it gave less vibration. (This is understandable since the dip in the cuvette overdetermines the axis, usually defined by the bearings, thus hindering performance.) Lubrification of the pivot bearing was provided by Pfeiffer 090 fluorinated Fomblin grease. The adjustable gap between rotor and stator was used in the range of 100–300 μm. When the gap size exceeds the interelectrode spacing, there is ambiguity as to which electrode is seen by a charged portion of the rotor so the device cannot function correctly. The motor would turn for a gap size of $\approx$300 μm but in general a somewhat narrower gap was used to provide higher torque. However, for spacings below 100 μm, parallelism of rotor and stator became a critical issue since even slight vibrations could halt operation.

Possibly because there was no air damping, configuration (i) proved to be dramatically unstable and was quickly abandoned. Results for the other three arrangements are presented below in Sec. IV B.

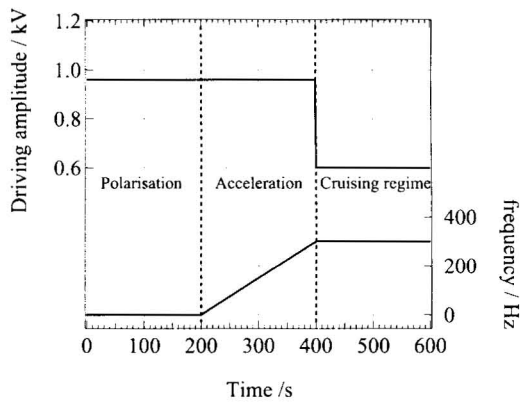

FIG. 6. Amplitude of driving voltage as a function of time. A dc polarization potential is followed by a three-phase driving signal whose amplitude is reduced once cruising speed has been obtained.

2. Driving voltages

The three-phase voltages necessary to drive the actuator are generated by three programmable synthesizers (Yokogawa FG 300) used in a master-slave configuration, the outputs of which are amplified by −120. The HV amplifiers employed at present (Apex Microtechnology AP89) with a gain-bandwidth product of 10 MHz provide a maximum amplitude of ±600 V at the 17 Hz rotation speed. The sequence currently employed is shown in Fig. 6. First, the glass rotor is polarized for 200 s at a dc potential of 480 V. Next, a sinusoidal voltage of peak-to-peak (p.-p.) amplitude of 960 V is applied during the acceleration phase lasting a further 200 s. Once the cruising rotational frequency of 17 Hz is reached, the electrical signal is maintained at 1020 Hz (corresponding to 17 Hz times the number of poles) but its p.-p. amplitude is reduced to 600 V.

B. Operation and characterization

In the atomic fountain, a photodiode located above the turbine detects residual transmitted light. Since the level of attenuation varies as the turbine turns, the photodiode current is modulated, which allows one to monitor the running of the device *in situ*. Before the installation of a working actuator in the atomic fountain, however, different designs were tested in an auxiliary vacuum system consisting of a stainless steel

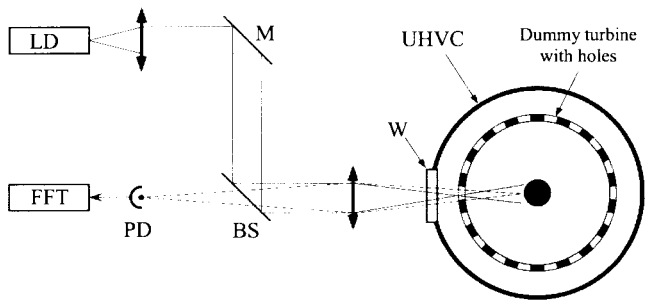

FIG. 7. Setup used to measure rotation frequency and vibration of the electrostatically driven turbine. Plain lines: illumination, focused on the turbine, dashed lines: detection light. (BS) beam splitter, (LD) visible laser diode, (M) mirror, (PD) photodiode, (UHVC) vacuum chamber, and (W) window.

chamber evacuated by an ion pump to about 10^{-8} mbar (Fig. 7) though with no cesium vapor present.

The vessel contained windows to allow observation of the motor and access of a visible laser beam for diagnostic purposes. To achieve the desired vacuum, the system was first evacuated using a turbo-molecular pump and baked to 100 °C before the ion pump was used alone. In this way, the thermal tolerance of the actuator was verified at an early stage.

To avoid potential damage to the glass turbine, a dummy load of identical moment of inertia was used for most of the developmental work (Fig. 8). It consisted of an inverted hollow dish made from aluminium whose circumference was perforated with 18 holes. Reflection of a visible laser diode and fast Fourier transform of the current from photodiode detector were used (cf. Fig. 7) to extract the rotation spectrum. By imaging the laser spot focused onto the spindle of the motor rather than the cylindrical surface of the turbine, we were able to obtain recordings of light level insensitive to the surface quality of the latter, the spindle acting as an effective point source of light emanating from within the turbine. Side lobes in the power spectrum either side of the main rotation frequency indicated the onset of vibrations. Indeed, the dummy allowed a finer analysis of vibrations than the glass bladed turbine would have done, in a way described in Sec. IV B 4 below.

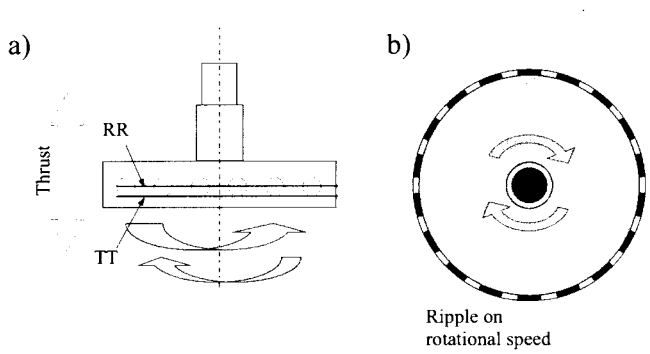

FIG. 8. Dummy turbine used for tests and types of vibration measured. (a) Side view. To show up tilt and thrust oscillations (TT), the height of laser impact was the lower edge of the holes. (b) Top view. For diagnostics of ripple of the rotation frequency (RR), a laser was reflected from the vertical center of the turbine.

1. Development procedure

The behavior of different configurations can be divided into three main categories. In the first, the motor accelerated but stalled before the desired rotation frequency was reached. To achieve a higher frequency required a greater couple, which was obtained by modification of the applied voltages and, if need be, reducing the gap between rotor and stator. In the second, the required angular frequency was attained but vibrations subsequently led to loss of synchronization (or occasionally to contact of rotor and stator). The mechanical configuration was modified as necessary. In the third case, the cruising speed was reached and maintained for the duration of the test. One could then choose the electrical parameters to minimize voltages in an effort to prolong the life of components. Once the final design had been adopted, the dummy turbine was replaced by the one with glass blades and the ensemble was tested for two weeks in the auxiliary vacuum chamber. It was then installed in the atomic fountain clock where it has been used on and off for several months under UHV in the presence of cesium at 10^{-8} mbar.

2. Measurement of the friction coefficient

Dry and viscous friction coefficients were measured to help optimize the choice of mechanical and electrical parameters. To this end, we suppose the system to be described by the following equation:

$$I\frac{d\omega}{dt} = \Gamma_m - k\omega - p\,\mathrm{sgn}(\omega), \tag{1}$$

where

$$\mathrm{sgn}(\omega) = \begin{cases} \omega/|\omega| & \text{for } \omega \neq 0 \\ 0 & \text{for } \omega = 0. \end{cases} \tag{2}$$

Γ_m is the torque applied by the motor, p and k, respectively, the dry and viscous friction coefficients. When the driving torque Γ_m is removed (i.e., the power supply is switched off), the angular velocity ω of the motor eventually falls from its initial value ω_i to zero. The decay constant provides the friction coefficient in different regimes. Specifically,

$$\omega(t) = \left(\omega_i + \frac{p}{k}\,\mathrm{sgn}(\omega)\right)e^{-kt/I} - \frac{p}{k}\,\mathrm{sgn}(\omega). \tag{3}$$

Note that if dry friction dominates, the rotational speed decreases linearly rather than exponentially,

$$\omega(t) = \omega_i - \frac{pt}{I}\,\mathrm{sgn}(\omega). \tag{4}$$

It is assumed in Eqs. (3) and (4) that ω does not change sign once its has fallen to zero. Results for three different configurations are as follows.

Thrust bearing plus single ball race. The system exhibits two regimes of behavior. Dry friction is dominant at rotation frequencies below 4 Hz with $p=4.4(0.8)\times 10^{-6}$ kg m^2 s^{-1}, while for faster rotation, it can be neglected but viscous friction is significant [$k=1(0.2)\times 10^{-7}$ kg m^2 s^{-2} measured at a pressure of 10^{-6} mbar]. Though an improvement over the version with no ball race (described above in Sec. IV A 1), this configuration was still

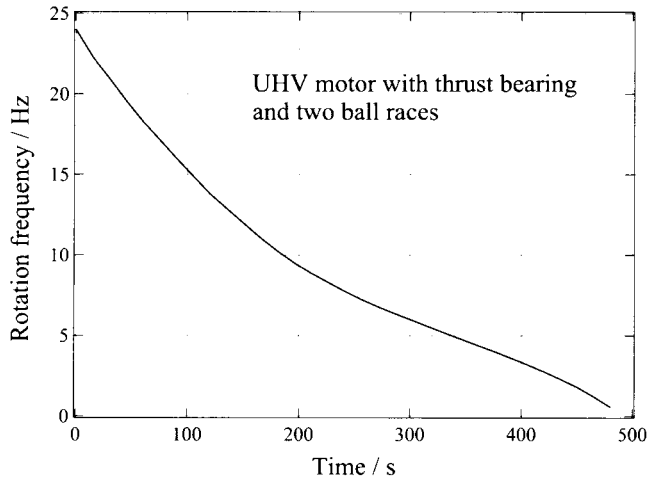

FIG. 9. A decay curve obtained under UHV for the configuration consisting of a thrust bearing and two ball races. Dry friction dominates below 4 Hz and viscous friction above it.

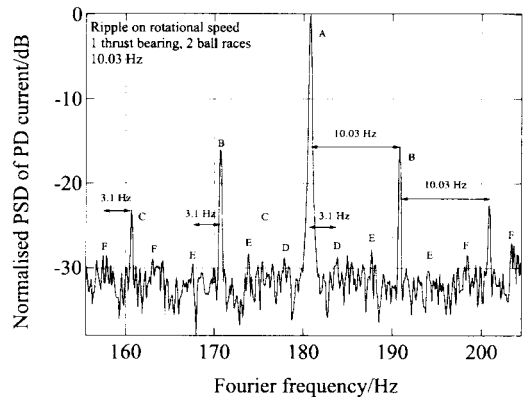

FIG. 10. Vibrational spectrum associated with ripple on the rotational frequency obtained under UHV for the configuration consisting of a thrust bearing and two ball races. The rotational frequency $f_{rot}=10.03$ Hz. (A) Main peak at $18f_{rot}$ (18 is the number of holes in the circumference of the dummy rotor); [(B) and (C)] sidebands offset by $\pm f_{rot}$ and $\pm 2f_{rot}$; [(D) and (E)] sidebands at 3.1 Hz due to vibrations.

too unstable for operation at 17 Hz where the motor often stalled. Consequently, no UHV-compatible version of this setup was ever constructed.

Thrust bearing plus two ball races. This more reliable configuration which could rotate at over 35 Hz was tested in both basic and UHV-compatible versions. A decay curve obtained at a pressure of 10^{-7} mbar is shown in Fig. 9. From an average of several measurements for $f<4$ Hz, we find $p=5.1(1.3)\times 10^{-6}$ kg m^2 s^{-2} and $k=6.3(3.0)\times 10^{-8}$ kg m^2 s^{-1}, while above 4 Hz, $p=1.27(1.3)\times 10^{-7}$ kg m^2 s^{-2} and $k=1.64(0.09)\times 10^{-7}$ kg m^2 s^{-1}, so at 17 Hz, $k|\omega|\gg p$ and one can neglect dry friction.

Two ball races only. In this case, the friction is essentially dry at all frequencies with $p=3(1)\times 10^{-5}$ kg m^2 s^{-2}, a value about ten times higher than for the version with a pivot and two ball races. However, this coefficient evolves rapidly as a result of wear on the bearings which here bear the whole load of the turbine. With a brand new ball race, a small amount of viscous friction was also measurable [$k=39.5(0.5)\times 10^{-9}$ kg m^2 s^{-1}].

3. Measurement of the maximum torque and rotational speed

The torque exerted by the actuator depends on the number and geometry of electrodes, a design parameter not quickly modified, as well as on the gap size and applied voltage, which one can vary easily. From a knowledge of the friction coefficients and rotation speed, one can deduce the value of the applied torque using Eq. (1). Measurements for the three different configurations above give $\Gamma_m=1.0(0.1)\times 10^{-4}$ N m. By setting $d\omega/dt=0$, one obtains the torque required to maintain a given rotational frequency,

$$\Gamma_m = k\omega + p\,\mathrm{sgn}(\omega). \tag{5}$$

For the configuration with a pivot and two ball races, the couple required to maintain rotation at 17 Hz is only $1.76(0.03)\times 10^{-5}$ N m. Thus, the torque available with the present motor is about six times this value, providing a margin of safety should friction increase through wear. As a corollary, the maximum rotation frequency predicted for this configuration would be about 100 Hz. In actual fact, the highest frequency observed was 60 Hz at which value stall occurred due to vibrations.

4. Measurement of vibrations

Even if sufficient torque is available to make the motor turn at a given frequency, the device can still be subject to stall caused by vibrations leading either to loss of synchronism or physical contact of rotor and stator. Three kinds of vibration occur in the type of actuator used here: ripple on the rotation frequency, i.e., around the axis, and tilt and thrust oscillations. If significant, the former kind can lead to an unacceptable loss of synchronism of rotor and stator, causing the motor to fail. At the same time, since the gap between rotor and stator is necessarily small, a large tilt or thrust oscillation could cause the rotor to touch the stator, with the risk of electrical failure or mechanical damage. We were able to distinguish between ripple and a combination of tilt and thrust by illuminating the dummy target at different heights. To highlight ripple on the rotation frequency, a laser beam was reflected from the vertical center of the turbine so as to be crossed by the middle of the holes (Fig. 8). To diagnose the combination of tilt and thrust oscillations, the height of laser impact was chosen to lie on the edge of these holes so that any vibration resulted in a significant change of the reflected intensity. Vibrational spectra were acquired mainly for the configurations using two ball races since only these reliably attained cruising speed. Measurements were made at frequencies from 5 to ≈ 30 Hz. For brevity, we summarize results for the UHV-compatible model with a pivot and two ball races rotating at the working speeds of 10, 17, and 28, or 30 Hz.

Ripple on the rotation frequency. The spectra are displayed in Figs. 10–12. The large peaks separated from the carrier by the rotation frequency could be caused by synchronous vibrations but equally arise from a variation of surface quality of the spindle or else a nonuniform angular separation of the holes in the dummy turbine. The smaller peaks, located a few hertz either side of the carrier, are due to ripple. More sidebands appear and become stronger for

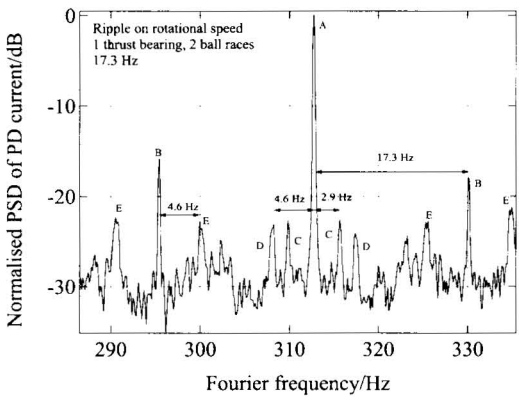

FIG. 11. Vibrational spectrum associated with ripple on the rotation frequency obtained under UHV for the configuration consisting of a thrust bearing and two ball races. The rotational frequency $f_{rot}=17.3$ Hz. (A) Main peak at $18f_{rot}$; (B) sidebands offset by $\pm f_{rot}$; [(C), (D), and (E)] sideband due to ripple.

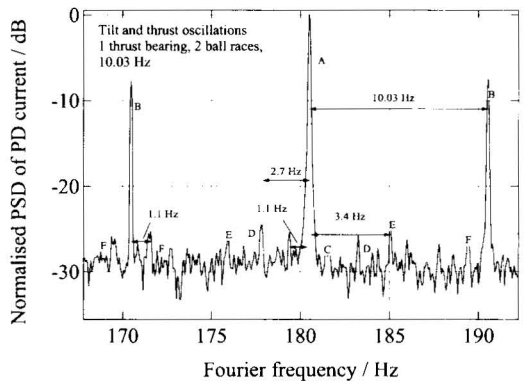

FIG. 13. Vibrational spectrum for a combination of tilt and thrust oscillations obtained under UHV for the configuration consisting of a thrust bearing and two ball races. The rotational frequency is 10.03 Hz. (A) main peak at $18f_{rot}$; (B) sidebands offset by $\pm f_{rot}$; [(C), (D), (E), and (F)] sidebands due to tilt/thrust.

higher rotational frequencies. For this type of oscillation, it is possible to deduce the amplitude of vibration from the relative power spectral densities of carrier and low-frequency sidebands in the Fourier spectrum of the reflected light (see Appendix). For example, at 17 Hz (Fig. 11), the 23 dB ratio implies an angular excursion $\delta\varphi_0=7.8$ mrad, about half of the critical value of 17 mrad at which decoupling is expected to occur. By contrast, at 30 Hz, this limit is almost attained for the sideband C at 2.7 Hz (Fig. 12).

Tilt and thrust oscillations. Spectra for tilt and thrust are shown in Figs. 13–15. Our method of measurement does not allow one to distinguish between these two types of oscillation. Vibrational sidebands due to one or other or both are present at a few hertz either side of the carrier. The theoretical model for ripple presented in the Appendix does not apply to this type of oscillation. We cannot therefore deduce the physical amplitude of motion from the ratio of sidebands to carrier in the Fourier spectrum. It is possible that these spectra also contain a contribution from ripple around 2.4–3.1 Hz as a result of cross-coupling.

5. Final configuration

Of the four configurations explored, only two proved sufficiently reliable at the rotation frequency of 17 Hz, namely, those containing two ball races. The version with a thrust bearing added is preferred first because of the lower load on the ball races that serve only for lateral guidance; the weight of the rotor and turbine is supported entirely by the bearing in this case. Second, the torque required to maintain rotation at 17 Hz is a factor of 2 lower.

6. Reliability, mechanical tolerances, and potential improvements

The electromagnetic stepper motors used in our previous light traps were dogged by bearing wear and the huge vibrations inherent to the principle of operation of such an actuator. In the case of the present electrostatic motor, an inherently smooth device, vibrations lie at an altogether smaller level, friction is minimal, and wear a far lesser issue. Indeed, measurements of the friction coefficient every few weeks have shown no sign of bearing wear. An added bonus has been the absence of outgassing, a troublesome side effect encountered with electromagnetic stepper motors containing

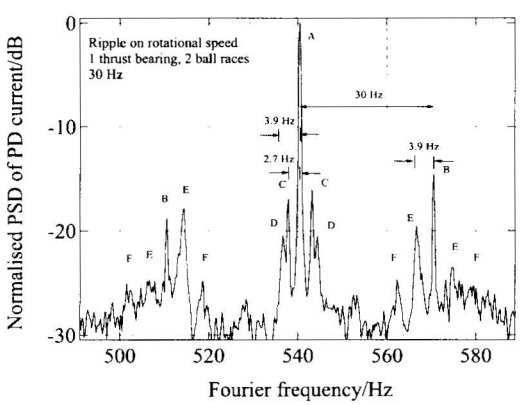

FIG. 12. Vibrational spectrum associated with ripple on the rotation frequency obtained under UHV for the configuration consisting of a thrust bearing and two ball races. The rotational frequency is 30 Hz. (A) Main peak at $18f_{rot}$; (B) sidebands offset by $\pm f_{rot}$; [(C), (D), (E), and (F)] sidebands due to ripple.

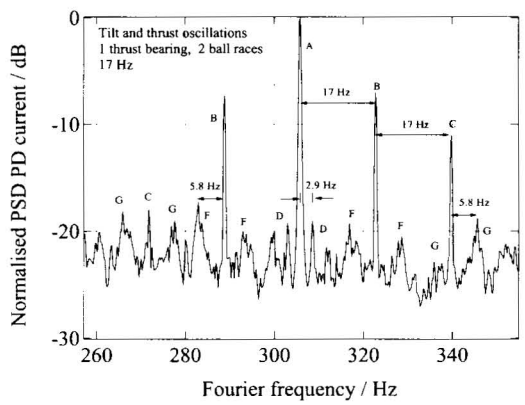

FIG. 14. Vibrational spectrum for a combination of tilt and thrust oscillations obtained under UHV for the configuration consisting of a thrust bearing and two ball races. The rotational frequency is 17 Hz. (A) main peak at $18f_{rot}$; [(B) and (C)] sidebands offset by $\pm f_{rot}$; [(D), (E), (F), and (G)] sidebands due to tilt/thrust.

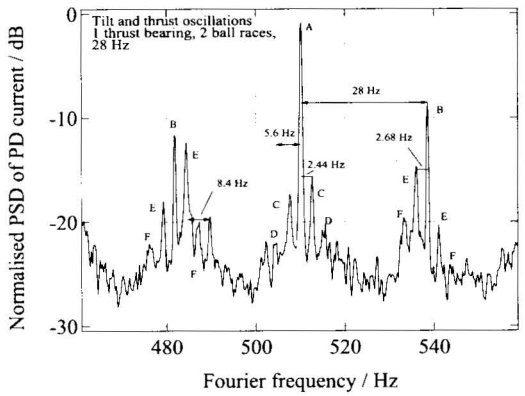

FIG. 15. Vibrational spectrum for a combination of tilt and thrust oscillations obtained under UHV for the configuration consisting of a thrust bearing and two ball races. The rotational frequency is 28 Hz.

lubricants. Even so, although a working prototype has been demonstrated, a setup with given dimensions usually requires some tweaking and does not necessarily work the first time. This is because the gap size of close to 100 μm is near the limit of mechanical tolerances. The flatness of the glass rotor is <5 μm and its eccentricity is <7 μm. By contrast, the electrodes are centered only to ±50 μm with respect to the axis of the stator. The radial tolerance of the assembled motor is at least as great. Any eccentricity leads to a reduced torque and is a potential source of vibration. Most serious, however, is the lateral play of 20 μm in the two ball races which, for a separation of 12.5 mm, corresponds to an angle of 3.2 mrad. This translates into a change in height of the circumference of the rotor of ±92 μm. A margin of comfort would be obtained if one used higher driving voltages so the gap size could be increased. Suitable HV amplifiers providing ±2 kV at 17 Hz are currently available (e.g., Trek model 677B). The fact one can increase the driving electric field without breakdown is an advantage of UHV operation compared with use at atmospheric pressure.

V. CONCLUSION

We have successfully designed, constructed and characterized a glass electrostatic actuator rotating continuously at 17 Hz for up to two weeks under UHV conditions (10^{-8} mbar). A maximum rotational frequency of 60 Hz was obtained. A velocity-selective light trap incorporating this device has now been implemented in a continuous cold-atom fountain clock. The demonstration of such a reliable, nonmagnetic actuator opens the way to a host of applications, notably where continuous fluxes of cold atoms are required, free of perturbations from magnetic fields and fluorescence from the source. Given that the requirements for a primary atomic clock are particularly stringent, the present type of actuator might find much wider use in less demanding situations, for instance, where 100% duty cycle is not an issue.

ACKNOWLEDGMENTS

The authors thank J.-F. Léchenne for expert technical assistance, G. Perruchoud for calculations of moments of inertia, and J. Guéna and C. Schori for critical reading of the manuscript. Partial financial support was provided by the canton of Neuchâtel and the Fonds national suisse de la recherche scientifique (FNRS). The generous support of the Gebert Ruf Foundation for the initial development of the electrostatic glass motor is gratefully acknowledged.

APPENDIX: PHASE MODULATION DUE TO RIPPLE ON THE ROTATION SPEED

The photodiode that monitors the light reflected from the inner hub of the dummy rotor, via the center of the N holes in its rim, yields a signal $S(t)$ consisting of trapezoidal pulses interspersed with blanks. Let ω_0 be the angular velocity of rotor and $\varphi(t)$ the angular position of the rotor with respect to the stator. Ripple on the rotation speed causes this angle to fluctuate by an amount $\delta\varphi(t)$,

$$\varphi(t) = \omega_0 t + \delta\varphi(t). \tag{A1}$$

If the trapezoidal pulses are approximated to square ones, Fourier analysis gives

$$S(t) = \frac{1}{2}A[1 + C(t)] = \frac{1}{2}A\left\{1 + \frac{4}{\pi}\sum_{k=0}^{\infty}\frac{1}{2k+1}\sin[(2k+1)\Phi(t)]\right\}, \tag{A2}$$

where

$$\Phi(t) = N(\omega_0 t + \delta\varphi(t)). \tag{A3}$$

Here, A is the amplitude and $C(t)$ is a square wave of average angular frequency $N\omega_0$ and whose value is ±1. The angular variation due to ripple at ω_m on the rotation frequency is

$$\delta\varphi(t) = \delta\varphi_0 \sin \omega_m t, \tag{A4}$$

where $\delta\varphi_0$ is the maximum angular excursion. If this exceeds half the angular size of the stator electrodes, the motor will stall. For the present stator with 180 electrodes, this implies that $\delta\varphi_0 < \pi/180 = 0.017$ rad. The excursion of the angular position at a given point on the rotor rim of radius R is $R\delta\varphi$. By combining Eqs. (A1)–(A4) one obtains

$$S(t) = A/2 + (A/8\pi) \times \sum_{k=0}^{\infty}\frac{1}{2k+1}\underbrace{\sin[(2k+1)N(\omega_0 t + \delta\varphi_0 \sin \omega_m t)]}_{\sin[\ ]}. \tag{A5}$$

Now,

$$\sin[\ ] = \sin[(2k+1)N\omega_0 t]\cos N\delta\varphi_0 \sin \omega_m t - \cos[(2k+1)N\omega_0 t]\sin N\delta\varphi_0 \sin \omega_m t, \tag{A6}$$

which can be expanded as

$$\sin[\ ] = \sin[(2k+1)N\omega_0 t]\sum_{p=-\infty}^{\infty} J_{2p}(N\delta\varphi_0)\cos 2p\omega_m t + \cos[(2k+1)N\omega_0 t]\sum_{p=0}^{\infty} 2J_{2p+1}(N\delta\varphi_0) \times \sin(2p+1)\omega_m t, \tag{A7}$$

where the J_{2p} are Bessel functions of order $2p$. If there were

no ripple ($\delta\varphi=0$), the spectrum would consist merely of all the odd harmonics of $N\omega_0$. In the case of interest here, however, $\delta\varphi \neq 0$, and each harmonic "carrier" at $N\omega_0(2k+1)$ is surrounded by side lobes at the ripple frequency ω_m, as expected. Since all "subspectra" of order k are identical, the discussion will be limited to $k=0$ (carrier $N\omega_0$). The fact that the real signal $S(t)$ is trapezoidal instead of square changes only the values of the Fourier coefficients $(2k+1)^{-1}$ and has no influence on the subspectra of order k. For $k=0$, and since with $N=18$, $N\varphi_0 \lesssim 0.3$ to avoid stalling, we retain only the dominant term in each Bessel function expansion ($p=0$), i.e., only the carrier $N\omega_0$ and first sidebands $N\omega_0 \pm \omega_m$. In this case, the expression for $S(t)$ reduces to

$$S(t) \approx (A/2)\{1 + (4/\pi)[J_0(N\varphi_0 \sin N\omega_0 t) + J_1(N\varphi_0) \times (\sin(N\omega_0 + \omega_m)t - \sin(N\omega_0 - \omega_m)t)]\}. \quad \text{(A8)}$$

The ratio η between the moduli of the amplitudes of the sideband and carrier is thus

$$\eta = \frac{J_1(N\varphi_0)}{J_0(N\varphi_0)} = \frac{N\delta\varphi_0}{2}. \quad \text{(A9)}$$

Hence, the maximum angular excursion is

$$\delta\varphi_0 = 2\eta/N. \quad \text{(A10)}$$

In other words, the square root of the ratio of the power spectral densities of carrier and sidebands gives a direct, self-calibrating measure of the angular ripple. By contrast, this approach cannot be used to analyze the combination of tilt and thrust oscillations.

[1] R. Moser and T. Higuchi, J. Electrost. **55**, 97 (2002).

[2] R. Moser, Ph.D. thesis, École Polythechnique Fédérale de Lausanne, Switzerland, 2002.

[3] R. Moser and T. Higuchi, Precis. Eng. **26**, 163 (2002).

[4] R. Moser, R. Wütrich, L. Sache, T. Higuchi, and H. Bleuler, J. Appl. Phys. **93**, 8945 (2003).

[5] R. Moser, L. Sache, A. Cassat, T. Higuchi, and H. Bleuler, IEEE Trans. Ind. Appl. **41**, 972 (2005).

[6] P. Thomann, M. Plimmer, G. Di Domenico, N. Castagna, J. Guéna, G. Dudle, and F. Füzesi, Appl. Phys. B: Lasers Opt. **84**, 659 (2006).

[7] R. Wynands and S. Weyers, Metrologia **42**, S64 (2005).

[8] S. Bize, P. Laurent, M. Abgrall, H. Marion, I. Maksimovic, L. Cacciapuoti, J. Grünert, C. Vian, F. Pereira dos Santos, P. Rosenbusch, P. Lemonde, G. Santarelli, P. Wolf, A. Clairon, A. Luiten, M. Tobar, and C. Salomon, J. Phys. B **38**, S449 (2005).

[9] T. Heavner, S. Jefferts, E. Donley, J. Shirley, and T. Parker, Metrologia **42**, 411 (2005).

[10] E. Tiesinga, B. J. Verhaar, H. T. C. Stoof, and D. van Bragt, Phys. Rev. A **45**, R2671 (1992).

[11] K. Gibble and S. Chu, Phys. Rev. Lett. **70**, 1771 (1993).

[12] S. Ghezali, Ph. Laurent, S. N. Lea, and A. Clairon, Europhys. Lett. **36**, 25 (1996).

[13] A. Joyet, G. Mileti, G. Dudle, and P. Thomann, IEEE Trans. Instrum. Meas. **50**, 150 (2001).

[14] A. G. Mann, C. Sheng, and A. N. Luiten, IEEE Trans. Instrum. Meas. **50**, 519 (2001).

[15] K. Szymaniec, W. Chałupczak, E. Tiesinga, C. J. Williams, S. Weyers, and R. Wynands, Phys. Rev. Lett. **98**, 153002 (2007).

[16] J. Guéna, G. Dudle, and P. Thomann, Eur. Phys. J.: Appl. Phys. **388**, 183 (2007).

[17] A. Joyet, G. Mileti, P. Thomann, and G. Dudle, in *Proceedings of the Seventh Symposium on Frequency Standards and Metrology, St. Andrews, Fife, Scotland, 9–14 September, 2001*, edited by P. Gill (World Scientific, Singapore, 2002), pp. 273–280.